Microscale nanosecond laser-induced optical breakdown in water

Sergey I. Kudryashov and Vladimir D. Zvorykin
P.N. Lebedev Physical Institute, Russian Academy of Sciences, Moscow 119991, Russia
(Received 29 December 2007; revised manuscript received 1 July 2008; published 17 September 2008)

Microscale optical breakdown induced in bulk pure water by high-power nanosecond KrF laser pulses was studied using optical transmission and contact broadband photoacoustic techniques. The breakdown has been identified as a sharp transmission drop coinciding with the appearance of unipolar compressive acoustic pulses, both indicating a thresholdlike rise of local intrinsic absorption in the micrometer-scale laser focal volume. The acoustic pulses, which are much broader than the exciting laser pulse and show a strongly reduced far-field diffraction effect, result from breakdown-induced millimeter-sized steam bubbles. The acoustic pulse amplitudes exhibit a sub-linear ($\propto I^{3/4}$) pressure dependence on the laser intensity I characteristic of subcritical electron-ion plasma and demonstrating the avalanche enhancement of two-photon ionization above the breakdown threshold until the appearance of the critical plasma. In the critical plasma regime, where the transmission and the acoustic signals slowly vary as a function of laser intensity, the main acoustic pulse is preceded by nanosecond and sub-μs prepulses, where the first one represents a GPa-level plasma-driven shock wave and the second one adjacent to the main pulse appears due to weak submillimeter-long heating of water surrounding the hot plasma by its bremsstrahlung radiation, indicating significant dissociation of water molecules in the plasma.

DOI: 10.1103/PhysRevE.78.036404 PACS number(s): 52.50.Jm, 61.80.Ba, 43.30.+m, 52.40.Hf

I. INTRODUCTION

Microscale optical breakdown in transparent liquids (mainly, water) is a key physical process for numerous applications and fundamental studies, such as shock-wave laser cleaning of nanometer-scale contaminants from critical substrates [1], laser microsurgery of microscopic organelles [2,3] and intracellular nanosurgery [4,5], laser ophthalmology—intraocular and intrastromal corneal refractive surgery [6,7], laser micropatterning of living animal cells [8], basic cavitation and shock-wave studies [9–12]. Various fundamental characteristics of optical breakdown in dielectrics were studied by means of optical shadowgraphy, diffraction, microscopy, interferometry, scattering and transient lens techniques [3,4,8,13–20], revealing informative spatiotemporal dynamics of post-breakdown phenomena (e.g., shock waves and vapor bubbles in liquids [3,4,8,13,15,18,21–23]), but providing, however, very limited insight into a crucial initial breakdown step—laser generation of optically opaque near-critical breakdown plasma—and its parameters because of the plasma screening effect. Moreover, acoustic techniques capable of detecting intense plasma-driven ultrasonic waves and insensitive to plasma screening were used so far mostly for tracking post-plasma nanobubble and microbubble formation and evolution, single measurements of shock-wave pressures, and acoustic generation thresholds [4,11,12,15,22–24]; only recently, a contact acoustic technique has been demonstrated to probe multiple informative parameters (plasma density and pressure, ionization mechanisms) of near-critical plasmas in solid dielectrics via their acoustic emission [25,26]. In the absence of accurate experimental data on parameters of laser-driven breakdown plasma in liquids, optical breakdown was usually quite arbitrarily associated with its various delayed attributes, such as shock waves [4,9–13,21–23], cavitation bubbles [4,9,13,21–23], or luminous plasma [21–23,27,28], not necessarily strictly related to corresponding breakdown thresholds, while estimates of plasma parameters based on experimentally measured characteristics of such subsequent breakdown attributes were until now the only source of our knowledge on breakdown plasmas.

Moreover, the development of the basic theory of optical breakdown in bulk dielectrics, which has started a few decades ago [29,30], is a still ongoing process [31], while some important issues, such as avalanche initiation and stopping, are not well understood yet. In particular, in liquids dissociation of their molecules—an analogue of self-trapping in solid dielectrics—can occur, besides ionization, during optical breakdown via direct collisions with hot electrons, ion- or radical-molecule chemical reactions [32], and absorption of uv bremsstrahlung plasma emission [23], efficiently competing with ionization due to the lower energy requirements (e.g., 6.6 eV for dissociation of water molecules against $\approx$12 eV for their ionization in a gas phase [32]). Hence, laser-induced generation of free radicals near a breakdown threshold could be not a miscellaneous channel, but the primary sink of laser energy in the corresponding prebreakdown regime. Both in solids and liquids, the "structural" induction effect entering common plasma dynamics models as a simple loss term [27,33], should temporally delay the electron avalanche onset and shift up the corresponding breakdown thresholds. However, so far this effect and its impact on a breakdown energy balance, as well as related cytogenic chemical effects [34] have not been considered within the present "amorphous solid dielectric" model of water [35].

More importantly, up to now there is no clear understanding of final evolution steps of a laser-driven electron avalanche. Usually, slowing down of an electron avalanche is supposed to occur at near-critical plasma densities because of the decreased laser energy input into an opaque, but strongly luminous subcritical plasma [36] changing its energy balance structure [37]. However, the detailed picture of such late evolution stage of an electron avalanche remains not well under-

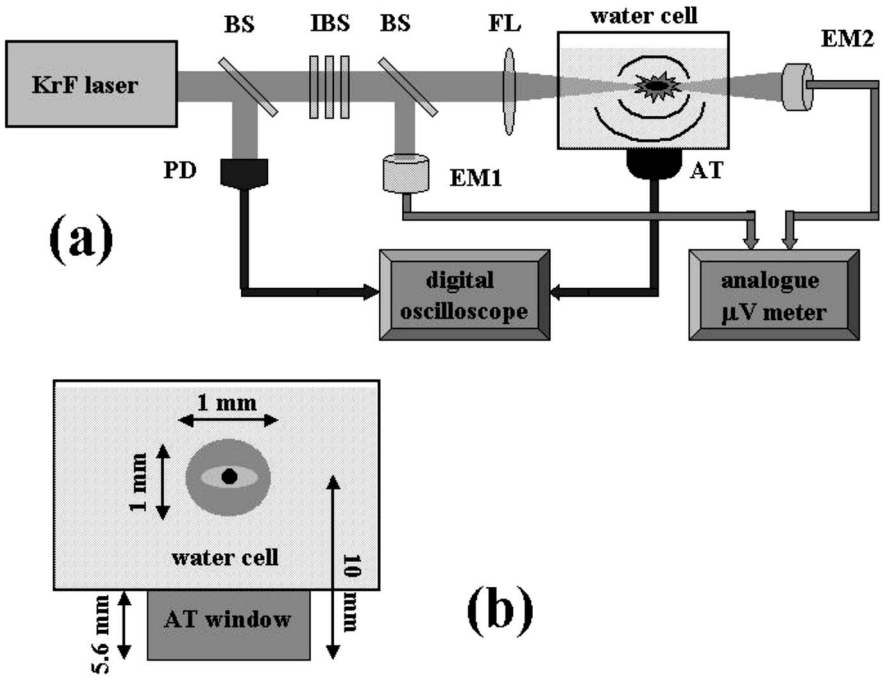

FIG. 1. (a) Experimental setup: BS and IBS, 45° ordinary and 0° interference (50%) beam splitters, respectively; FL, focusing lens; PD, photodiode; AT, acoustic transducer; EM1,2, calibrated energy meters. (b) Acoustic detection scheme with the steam bubble (dark gray circle), laser focal volume (gray ellipse), and plasma ball (black circle) in the water cell (dimensions not to scale).

stood yet because of (1) the above-mentioned experimental difficulties in optical probing of opaque plasma and (2) the existing gap between the well-developed kinetic models of electron avalanche ionization in dielectrics [29–31] and the well-established thermodynamic models of laser ionization and heating in near-critical plasmas [37], with the latter providing very useful multiparametric universal scaling relationships between basic plasma parameters (density, temperature, pressure) and incident laser intensities I, wavelengths, and pulse widths. For example, in a subcritical plasma regime very weak ($\propto I^{1/4}$) intensity-dependent increase of plasma density N_e takes place until formation of the critical plasma [37], drastically differing from the strong exponential-like rise of $N_e(I)$ during optical breakdown, according to the standard kinetic models [29–31]. Unfortunately, comparing to solid dielectrics [25,26], such subcritical and critical plasma regimes have not been identified yet during optical breakdown in liquids; as a result, the current knowledge of basic breakdown parameters, which are the initial conditions for the entire set of radiative, hydrodynamic, acoustic, thermal, and phase change events, is strongly limited.

Summarizing, the existing physical picture and corresponding theory of optical breakdown in liquids is apparently missing the important initial and final links associated with dissipative chemical (dissociation) and dense opaque plasma effects, which strongly affect the onset and completion of the breakdown electron avalanche, respectively. Experimental identification and investigation of these effects is very important for understanding of breakdown dynamics and evaluation of its basic parameters, and their influence on post-breakdown attributes—luminous plasma, shock waves, cavitation bubbles, and related modifications in biological organisms.

In this work we use optical transmission and contact broadband photoacoustic techniques to study microscale optical breakdown of pure water and variation of basic parameters (wave-form shape, arrival time, time width, amplitude) of the acquired acoustic transients as a function of incident laser intensity. These experimental results enable us to identify and characterize the breakdown and succeeding subcritical and critical plasma regimes in terms of their thresholds, plasma pressures and densities, and relate them to specific breakdown features, such as a rise of bremsstrahlung plasma emission, an appearance of a shock wave and a steam bubble, demonstrating significant dissociation of water molecules in the near-critical plasma and surrounding water.

II. EXPERIMENTAL SETUP AND TECHNIQUES

A 248-nm KrF laser beam [Lambda Physik EMG150, the maximum pulse energy $E_0 \approx 0.12$ J, full width at half-maximum (FWHM) Gaussian pulse width $\tau_{las} \approx 25$ ns, repetition rate of 1–200 Hz] was used to irradiate bulk doubly distilled water (Oilright, Tektron) contained in a cell (width $x_{cell} \approx 10$ mm, height $y_{cell} \approx 10$ mm, and length $z_{cell} \approx 20$ mm) with 3-mm-thick input and output fused silica (FS) windows [Fig. 1(a)]. The beam was focused inside the water cell at normal incidence by a 7-cm focal length lens into a focal spot $x_{las} \times y_{las} = 40 \times 80$ μm^2 (the estimated Rayleigh length $z_{las} \approx 800$ μm) with rectangular and Gaussian distributions of fluence F along horizontal x and vertical y axes, respectively. Laser energy was varied in the range $(0.01-1)E_0$ using a number of interference beam splitters (50% attenuation per piece) and was measured in each pulse by splitting off a part of the beam to a thermocouple energy meter (VChD2, OKB FIAN).

The other same detector was used to measure the laser pulse energy transmitted through the water cell in order to derive its spatially and temporally averaged transmission T at the laser wavelength as a function of laser energy. The averaging results from the y-axis Gaussian laser beam inhomogeneity, its focusing along the z axis inside the water, and the

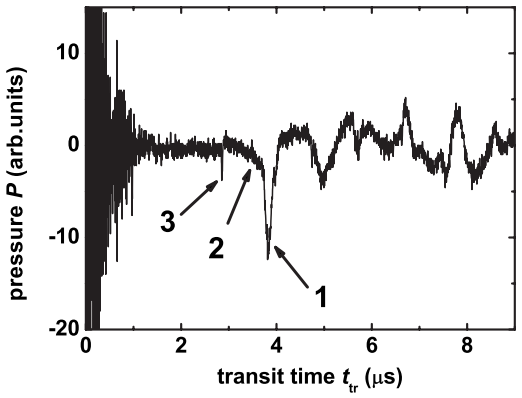

FIG. 2. Characteristic acoustic transient $P(t_{tr})$ in water at laser fluence $F \approx 1.7 \times 10^3$ J/cm^2. The initial signal spikes near the zero time instant represent electromagnetic noise of the laser gas discharge, while the arrows show the main compressive pulse (1), the broad (2) and narrow (3) prepulses.

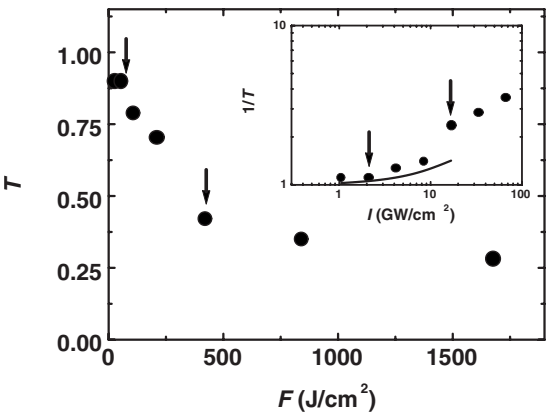

FIG. 3. Average optical transmittance T of the water cell versus F. Inset: The experimental dependence $1/T - \ln I$ and the estimated TPA contribution (solid line). The arrows in both figures show the subsequent thresholds for breakdown (F_{break}) and saturation (F_{sat}), respectively.

time-integrating detector, thus providing experimental T readings averaged over the time period from the beginning of the Gaussian laser pulse and the entire water cell volume V,

$$T(E) = 1 - R(E) - A(E) \approx 1 - (1 - R_{aFS})^2(1 - R_{FSw})^2 \times \oint_V^{\infty} \int_0 (\alpha + \beta I + \gamma N_e + \delta N_{rad}) I/E dV dt, \quad (1)$$

where $T(E)$, $R(E)$, and $A(E)$ are the average transmittance, reflectance, and absorbance of the water cell at the laser pulse energy E, $R_{aFS} \approx 0.04$ and $R_{FSw} < 0.01$ are the 248-nm reflectances at air-FS and FS-water interfaces (the corresponding refractive indexes $n_{FS} \approx 1.5$, $n_w \approx 1.4$ [38,39]), α, βI, γN_e, and δN_{rad} represent the relevant dissipation processes such as linear absorption, two-photon absorption (TPA) [40] at the incident laser intensity I leading to dissociation or ionization (TPI) of water [32], and absorption of the laser-generated free carriers (FCA) [36] and radicals [41,42] with their concentrations N_e and N_{rad}, respectively. Here, absorbance of the FS windows and the intrinsic reflectance change in the laser-excited water were neglected [13].

A front FS slab (thickness $h \approx 5.6$ mm) of a fast acoustic transducer SHAPR-04 ($LiNbO_3$ piezoelement with the 1.5-mm wide surface electrode, flat response in the frequency range $f \leq 100$ MHz, sensitivity of 0.9 mV/bar, UC VINFIN) [43] served as a bottom of the water cell. The 50-Ω inputs of a Tektronix storage oscilloscope (TDS 2024) were used to receive trigger pulses from a fast photodiode (DET210, Thorlabs) and signal pulses from the transducer. The recorded acoustic transients $P(t_{tr})$ were delayed regarding the trigger pulses and high-frequency laser discharge electromagnetic noise (Fig. 2) by transit times t_{tr} required for the transients to propagate in water (the path $y_{break} \approx 4.4$ mm) and the 5.6-mm-thick FS slab from the laser deposition region inside the water cell to the transducer [Fig. 1(b)]. The relatively small dimensions ($x_{las}, y_{las}, z_{las}$) of the laser focal volume in water were expected to provide data acquisition in the acoustic far field. Then, acoustic diffraction results in differential shapes of the recorded transients, according to the estimated dimensionless diffraction parameter $(y_{break}/L_{D,w} + h/L_{D,FS}) \sim 10$, where $L_{D,w/FS}(40\ \text{MHz}) \approx x_{las} z_{las}/C_{l,w/FS}\tau_{las} \approx 1$ and 4 mm are the diffraction lengths in water and FS [44], respectively, calculated for the characteristic laser pulse frequency component $f_{las} \approx 1/\tau_{las} \approx 40$ MHz, and the corresponding longitudinal speeds of sound $C_{l,w} \approx 1.5$ km/s and $C_{l,FS} \approx 5.9$ km/s [38]. Also, for the known values of nonlinear attenuation coefficient for water, $\alpha/f^2 \approx (2.42-2.5) \times 10^{-14}$ s^2/m for $f = 7-1.9 \times 10^2$ MHz [38], even multi-MHz components ($f < 100$ MHz) of the acoustic transients were not subject to considerable attenuation when propagated the distance $y_{break} \approx 4.4$ mm in water. Acoustic reverberations in the FS slab and water volume with periods in the range 2–8 μs were out of our 1-μs acquisition time window at $t = 3.25-4.25$ μs, with the latter covering only ballistic transit times for the acoustic transients (Fig. 2).

Importantly, the transmission and photoacoustic techniques used in this study were complementary, providing us with not only a quantitative measure of overall transmitted laser energy, but also important transient details of the corresponding nonlinear laser absorption in the water.

III. EXPERIMENTAL RESULTS

A. Optical transmission studies

The optical transmission measurements show at low incident laser fluences $F \leq 50$ J/cm^2 ($I \leq 2$ GW/cm^2) the nearly unperturbed water cell transmittance, $T_0 \approx 0.9$ (Fig. 3), determined presumably by the interface reflectances R_{aFS} and R_{FSw}. In this fluence range water absorbs via two-photon process (TPA) with the crossover from fluence-independent linear absorption to TPA occurring at much lower $F < 1$ J/cm^2 ($I < 0.02$ GW/cm^2) [45]. The minor variation of T in Fig. 3 is consistent with the low uv TPA coefficient in water, $\beta(264\ \text{nm}) \approx 0.5$ cm/GW [40], providing for $I \sim 1$ GW/cm^2 the increase $\Delta(1/T) \approx (1 + \beta I d) - 1 \sim 0.01$ (Fig.

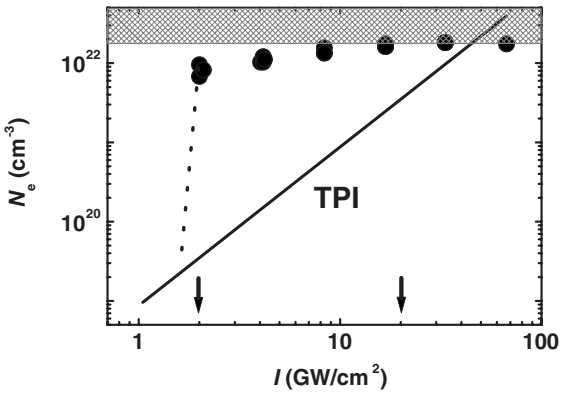

FIG. 4. $N_e(I)$ curves calculated using the photoacoustic data (dark circles) and TPI parameters (TPI, solid line), respectively, for the intensity range between the thresholds I_{break} and I_{sat} marked by the arrows. The expected breakdown trajectory is given by the dotted line and the shadowed region represents the critical plasma with $N_{cr}(248\ \text{nm}) = 1.8 \times 10^{22}\ \text{cm}^{-3}$.

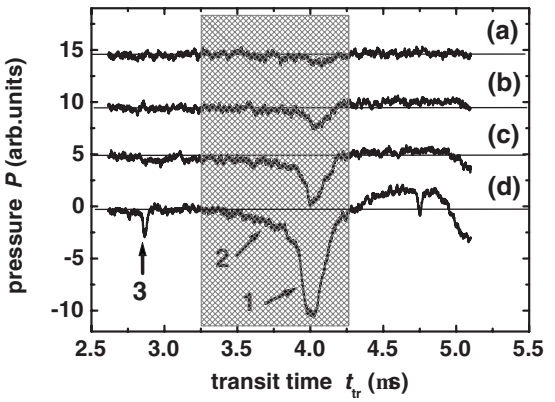

FIG. 5. Acoustic transients $P(t_{tr})$ in water at different KrF laser fluences (J/cm^2): 105 (a), 210 (b), 420 (c), and 1680 (d). The arrows show the main compressive pulse (1), broad (2) and narrow (3) prepulses, and the shadowed region represents the 1-μs acquisition time window.

3, inset) over the effective TPA length in water $d = z_{las}/2^{1/2} \approx 0.5\ \text{mm} \ll 1/(\beta I)$. The 248-nm TPA in water results presumably in ionization, rather than dissociation of water molecules, yielding the ion-radical ratio ≈ 10 [32].

At higher $F = (0.5-4) \times 10^2\ \text{J/cm}^2$ the T magnitude demonstrates a sharp decrease (rise of $1/T$) exhibiting an exponential-like laser-induced absorption [46] stronger than TPA (Fig. 3, inset), under the irradiation conditions typical for nanosecond laser breakdown in liquids [22]. The underlying potential absorption channels in the laser-irradiated water are: (1) the considerable absorption of OH radicals [41] ($\alpha_{OH} \approx 420\ \text{cm}^{-1}/\text{mole}$ for the $X\,^2\Pi_i \rightarrow A\,^2\Sigma^+$ transition at 267 nm [42]) generated via dissociation of water molecules through TPA, as well as through single-photon absorption of uv fraction of bremsstrahlung plasma emission, electron impact, ion- and radical-molecule reactions (see Sec. IV); (2) linear FCA in dense water plasma produced under the typical breakdown conditions [13,22,46,47] via an avalanche process from the TPI-generated electron-ion plasma with concentration $N_e > 10^{19}\ \text{cm}^{-3}$ (Fig. 4) estimated, using the above-mentioned laser pulse and β parameters, and the effective first ionization potential in liquid water, $I_{p1}(l\text{-}H_2O) \approx 10$ eV [32]. This drop of T is related in this work with an onset of optical breakdown in the laser-excited water at the threshold value $F_{break} \approx 50\ \text{J/cm}^2$ (Fig. 3), in agreement with our photoacoustic results presented below.

Finally, there is a slower decrease of T in Fig. 3 for $F > F_{sat} \approx 4 \times 10^2\ \text{J/cm}^2$ ($I_{sat} \approx 16\ \text{GW/cm}^2$), which can be explained either by recombination- [19,36,48] or self-regulated absorption and/or transmission [37] in dense near-critical or critical plasmas or by filamentary propagation of the uv laser pulses with supercritical powers in water [49]. First, radiative two-body [19,36] or radiationless three-body Auger [48] recombination processes may become effective under these irradiation conditions in the near-critical plasmas in water [the lower bound $N_e \sim 10^{21}-10^{22}\ \text{cm}^{-3}$ (Fig. 4) estimated in the assumption of presumable TPI]. The recombination processes may strongly limit FCA providing much slower intensity-dependent increase of plasma density $N_e(I)$ $\approx \sqrt[2]{G_{ion}(I)/\beta_{rad}}$ for radiative recombination and $N_e(I) \approx \sqrt[3]{G_{ion}(I)/\gamma_A}$ for Auger recombination, where $G_{ion}(I)$ is the laser ionization term, $\beta_{rad} \sim 10^{-9}\ \text{cm}^3/\text{s}$ [19] and $\gamma_A \sim 10^{-30}\ \text{cm}^{-3}/\text{s}$ [47] are the characteristic radiative and Auger recombination coefficients, respectively. Alternatively, self-focusing of the incident uv laser pulses with near-critical peak powers $P = 0.6-2\ \text{MW} \sim P_{crit}$ (the critical power P_{crit} in water varies from 1.15 MW at 527 nm [13,49] to 4.4 MW at 800 nm [16]) may result in filamentary propagation of the laser pulses stabilizing ionization and transmission dynamics in water in this fluence range. Finally, the slow decrease of T for $F > F_{sat}$ can be interpreted as the self-regulating absorption-transmission regime [37] in the subcritical water plasma ($N_e \sim 10^{21}-10^{22}\ \text{cm}^{-3}$) transparent at 248 nm [the critical plasma density $N_{cr}(248\ \text{nm}) \approx 1.8 \times 10^{22}\ \text{cm}^{-3}$, being close to the molecular density of normal liquid water, $N_{mol} \approx 3.3 \times 10^{22}\ \text{cm}^{-3}$]. More detailed insight into this fluence-dependent variation of T is provided below by the complementary photoacoustic studies.

Surprisingly, the observed fluence-dependent uv transmittance variation in Fig. 3, when plotted versus F/F_{break}, is in semiquantitative agreement with results of previous similar measurements, performed with nanosecond visible and ir laser pulses [13]. This indicates that optical breakdown in water has a universal character over the broad spectral range of nanosecond laser wavelengths.

B. Photoacoustic studies

In this work, acoustic pressure transients $P(t_{tr})$ were first acquired for $F \geqslant F_{break} \approx 50\ \text{J/cm}^2$, while no acoustic signal was observed at lower $F \leqslant 25\ \text{J/cm}^2$ (Figs. 5 and 6). These transients arrived to the transducer at $t_{tr} \approx 3.85\ \mu$s (Fig. 5) dictated by the transit times in water and the FS slab—2.9 μs for the water path $y_{break} = 4.4 \pm 0.1$ mm and 0.95 μs for the slab thickness $h = 5.6 \pm 0.1$ mm—at the longitudinal speeds of sound $C_{l,w} \approx 1.5$ km/s and $C_{l,FS} \approx 5.9$ km/s [38], respectively (the FS slab transit time has been independently verified directly ablating a dry 50-μm-thick aluminum foil, at-

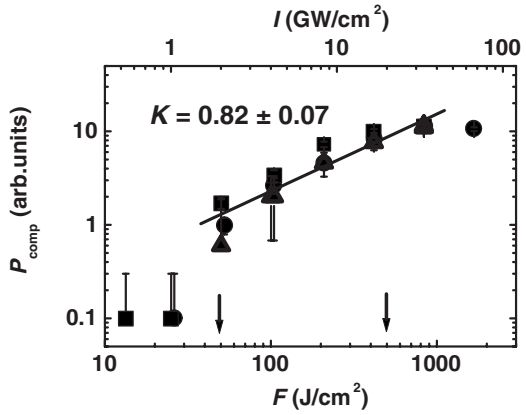

FIG. 6. Amplitude P_{comp} of the main compressive acoustic pulses measured in three independent series (dark squares, circles, and triangles) as a function of F and I. The value K represents the slope of the linear curve fitting this dependence in the range between the thresholds I_{break} and I_{sat} marked by the arrows.

tached to its surface, with a transit time less than 10 ns). Hence, the transients represent laser-generated sonic waves coming from the spatially well-defined acoustic source in bulk water within the cell, while the source coincides with the laser focal volume. Surprisingly, their wave forms $P(t_{tr})$ exhibited single, low-amplitude 100-ns broad (much broader, than the 25-ns laser pulse FWHM) compressive pulses [Fig. 5(a)], rather than the characteristic far-field bipolar pulses expected from the acoustic diffraction considerations in Sec. II; the potential reasons for this discrepancy are considered below. For $F \leqslant F_{break}$ the pulse amplitudes P_{comp} demonstrate a high slope in double logarithmic coordinates $\ln P_{comp}$-$\ln I$ (Fig. 6), which is characteristic of a nonlinear rise of local absorption of laser energy in water and is consistent with the results of our transmittance measurements exhibiting optical breakdown in water. The detailed mechanism underlying generation of the compressive acoustic signals is discussed in Sec. IV.

At higher fluences $F > F_{break}$ the acoustic pressure wave forms $P(t_{tr})$ show similar, but much more intense main compressive pressure pulses [Fig. 5(b)], indicating the qualitatively similar acoustic generation dynamics in water over the entire fluence range. However, now their amplitudes P_{comp} plotted in the $\ln P_{comp}$-$\ln I$ coordinates (Fig. 6) demonstrate much slower—sublinear—increase as a function of I, which can be described well in the range $I_{break} \leqslant I \leqslant I_{sat}$ by a single curve with a slope $K = 0.82 \pm 0.07$. This slope is characteristic of a universal scaling relationship between plasma pressure P_{plas} and incident laser intensity I in subcritical one (1D) or two-dimensional (2D) plasmas with the predominant FCA, where for 1D plasma $K = 0.75$, $P_{plas,subcr} \sim N_e k_B T_e \propto I^{3/4}$ for the plasma density $N_e \propto I^{1/4}$ and plasma thermal energy per particle $k_B T_e \propto I^{1/2}$, while for 2D plasma $K = 0.78$ [37]. The fact that the pressure in our water plasma apparently follows this scaling relationship indicates that this subcritical plasma regime is achieved in this work for $F > F_{break}$ with laser energy deposition and water ionization proceeding presumably via FCA [36,46] and plasma-mediated impact ionization [36], rather than TPA and TPI, respectively. This gives an additional supporting evidence of water breakdown for $F \approx F_{break}$, with the latter corresponding to the transition point between the free avalanche and plasma-mediated impact ionization regimes and thus providing the upper bound for the water breakdown threshold.

At even higher fluences $F > F_{sat}$ the main compressive pressure pulses preserve their temporal shapes $P(t_{tr})$, but additional low-amplitude narrower (FWHM $= 30 \pm 2$ ns) compressive pre-pulses and broader (sub-μs-long) exponential-like compressive prepulses and rarefaction post-pulses emerge simultaneously, preceding and succeeding the main pulses [Figs. 5(c) and 5(d)]. The narrow prepulses arriving almost 1 μs ahead of the corresponding main pulses (Figs. 2 and 5) may represent acoustic waves originating from initial plasma-driven shock waves, which propagate from the plasma source in water initially at supersonic speeds (their average speed over the 4.4-mm water path ≈ 2.4 km/s $> C_{l,w} \approx 1.5$ km/s) eventually slowing down due to the radial diffraction and dissipative attenuation [12,22] of their initial pressure $P_{plas,cr}$ (see Sec. IV for P_{plas} estimates). In contrast, the broad compressive prepulses resemble both in durations and amplitudes the compressive acoustic prepulses produced in water layers of similar thickness via their bulk heating by a thermal radiation (photon energies <6 eV) from surface plumes or ablation (breakdown) plasmas during irradiation of water surfaces by a TEA CO_2 laser [50]. In this case, the appearance of such broad prepulses for $F > F_{sat}$ may indicate a sharp onset of a plasma bremsstrahlung emission with its weakly absorbed sub-6-eV spectral components leaking in water at sub-mm distances from the plasma source [50], while the other, shorter-wavelength components are strongly absorbed by water molecules inside the plasma and in its proximity, providing their dissociation [51].

The main pulse amplitudes P_{comp} show their saturation in this irradiation regime (Fig. 6), consistent with the slower decrease of the average water transmittance in the fluence range in Fig. 3. Moreover, the amplitudes of the preceding narrow shock pulses increase approximately as $\propto I^{2/3}$, as expected for critical plasmas [37], being consistent with their 30-ns FWHM, which is exactly $(3/2)^{1/2} \approx 1.2$ times longer than the 25-ns FWHM of the Gaussian laser pulse profiles. The lower bound $N_e \approx 10^{22}$ cm^{-3} estimated for $F > F_{sat}$ considering the only TPI contribution (Fig. 4), supports the relation of the slowly changing main acoustic and transmittance signals to formation of the opaque critical plasma. Since such plasma is strongly absorbing and luminous with its thermal energy density rapidly increasing versus I [37], we believe that it is its formation rather than optical breakdown (an avalanche-like increase of plasma density) [4,12,13,21–23,27,28], that is responsible for the dramatically enhanced radiative bremsstrahlung energy transport out of the plasma and for the appearance of the plasma-driven shock waves. The other potential explanations of the above-mentioned trends for the transmittance and acoustic signals—filamentation and recombination—both do not exclude formation of critical plasma [25,49] with the radiative or Auger recombination processes counteracting impact ionization and thus providing smooth variation of N_e versus I in dense plasmas [36,48].

As an additional support of our photoacoustic results, similar compressive acoustic wave forms and their ampli-

tudes were earlier acquired, using a contact piezoelectric transducer, as a function of energy of single femtosecond and picosecond laser pulses tightly focused into bulk pure water [15]. The similar slope $\approx\frac{3}{4}$ can be seen from these energy dependences of the compressive pressure amplitudes obtained for both of these cases in the broad ranges of pulse energies—$1-10^2$ μJ and $10-10^2$ μJ, respectively, representing the characteristic subcritical (opaque) plasma regime, as discussed above and directly revealed by time-resolved optical microscopic imaging [15,18]. Likewise, at lower pulse energies both these energy dependences increase in a nonlinear manner consistent with either multiphoton absorption, or optical breakdown, while at higher energies ($\approx 10^2$ μJ) tend to saturate showing a lower slope [15], as expected for critical plasmas [37].

IV. DISCUSSION

A. Parameters of laser microplasma and ionization mechanisms in water

As mentioned above, the slope $K\approx 0.8$ in Fig. 6 indicates the subcritical character of microplasma in water for $I_{\text{break}}<I<I_{\text{sat}}$, similarly to the photoacoustic observations in Ref. [15] for femtosecond and picosecond laser pulses. More exactly, in this laser intensity range the subcritical plasma density increases as $N_e\propto I^{1/4}$ until the transition to the critical plasma showing another trend ($N_e=N_{\text{cr}}$) [37]. Likewise in Ref. [15], we observe this transition to the critical plasma in water at higher $I\geqslant I_{\text{sat}}\approx 16$ GW/cm^2 (Fig. 6), where the slope of the $P_{\text{comp}}(I)$ curve dramatically changes, being accompanied by the shock-wave emission and the onset of enhanced plasma bremsstrahlung emission, as well as by the much slower decrease of T in Fig. 3. Having this transition point as a reference, the subcritical plasma density N_e was calculated as a function of I as $N_e(I)=N_{\text{cr}}(248\text{ nm})(I/I_{\text{sat}})^{1/4}$ demonstrating values $N_e\sim 10^{22}$ cm^{-3}. Our auxiliary experiments on laser irradiation of a free water surface under the same experimental conditions, which have exhibited distinct formation of surface luminous plasma and expulsion of a water jet, also support the plasma density estimates, since for the explosive boiling in water energy densities $\varepsilon\sim N_e I_{p1}(g\text{-}H_2O)\geqslant 1$ kJ/cm^3 are required [43,52] provided in this case at $N_e\sim 10^{21-22}$ cm^{-3} for the first ionization potential of gaseous water molecular $I_{p1}(g\text{-}H_2O)\approx 12$ eV [51].

The calculated curve in Fig. 4 demonstrates for $I\approx I_{\text{break}}$ more dense plasma, than that expected from the pure TPI contribution, in agreement with the highly nonlinear rise of $1/T$ in Fig. 3 (inset). Hence, one can conclude on the breakdown origin of this subcritical plasma and the extremely sharp rise of $N_e(I)$ at $I\leqslant I_{\text{break}}$, associated mostly with the electron impact (avalanche) ionization mechanism [22], since another alternative—tunnel—ionization process is negligible at these relatively low I values corresponding to the laser electric fields much lower than characteristic interatomic ones. At higher $I_{\text{break}}<I<I_{\text{sat}}$ the plasma density is regulated by the thermodynamic relationship $N_e\propto I^{1/4}$ [37] with the dominating electron impact ionization mechanism balanced by radiative and Auger recombination.

B. Post-breakdown acoustic generation mechanisms in water

Main post-breakdown acoustic generation mechanisms in liquids are usually associated with plasma-driven shock waves and repetitive acoustic transients from thermal cavitation bubbles optically visualized in laser-irradiated liquids [4,12,13,21–23]. In this study using the broadband contact photoacoustic technique, we observed—about 1 μs prior to the main compressive acoustic pulses—the narrow acoustic prepulses representing the initial plasma-driven shock waves. Their 30-ns FWHM indicates quasistatic heating of the critical water plasma preceding the corresponding shock waves, since the scaling relationship $P_{\text{plas,cr}}\propto I^{2/3}$ [37] corresponds to temporal broadening of the prepulses, as compared to the 25-ns FWHM Gaussian laser pulse, exactly by $(3/2)^{1/2}\approx 1.2$ times, as expected from the power slope of $2/3$. Such heating process is typical for ns laser heating of subcritical and critical plasmas in ablative plumes, providing their presumable extension toward the laser source [53], but is also in surprising agreement with the strongly elongated shapes of breakdown plasmas in liquids [12,21–23] (see also the downstream moving breakdown model in Ref. [22]), thus, potentially, indicating the universal character of the ns laser-induced optical breakdown in vapor plumes and bulk liquids.

The other aspect of the quasistatic laser heating of the critical plasma is inhomogeneity of the resulting spatial energy distribution, exhibiting a hot plasma core and a surrounding shell of less dense and cooler expanding plasma [53], in contrast to the "sharp step" model of the breakdown plasmas [4,12,13,19,21–23] (note that for femtosecond laser-induced plasma in water the plasma heating and expansion processes are separated in time [18]). This leads to considerable radial pressure gradients in the plasmas requiring a certain onset time for a nonlinear front steepening in an emerging acoustic wave and appearance of a shock wave with the characteristic "sharp front plus long tail" structure [54]. Hence, in inhomogeneous microplasmas rapid divergence of the emerging acoustic wave may result in its considerable attenuation counteracting or preventing the shock-wave appearance, though the resulting high-amplitude acoustic wave will propagate at supersonic speeds. This appears to be the case in this study, according to the FWHM and amplitude characteristics of the acquired narrow prepulses.

Moreover, such spatial inhomogeneity of the breakdown critical plasmas imposes some limitations during optical measurements of various plasma parameters, since the visible plasma rim is only the apparent (effective) external edge of the opaque plasma. As a result, in optical measurements of shock-wave speeds extrapolated further to the plasma rim [12,22,23], the resulting calculated plasma pressures might be somewhat underestimated because of the expected internal pressure gradients in the plasma. Moreover, exact radial attenuation relationships $P(r)\propto 1/r^k$ should be generally known for initial spherical, cylindrical or other arbitrary shapes of corresponding plasma sources [12] and all relevant pressure ranges [12,38], while this information is very limited up to date. In contrast, the above-mentioned universal scaling relationships for the pressure P_{plas} in near-critical plasmas, though generally suffering from the absence of absolute calibration, can describe variations of the plasma and

related shock-wave pressures in a broad range of basic laser parameters (intensities, wavelengths, and pulsewidths [37]) and can provide useful estimates of P_{plas}. For example, in our case at $I_{sat} \approx 16$ GW/cm^2 one can estimate $P_{plas,cr} \sim N_{cr} k_B T_e \sim 10^5$ bar for $N_{cr}(248\ \text{nm}) \sim 10^{22}$ cm^{-3} and $k_B T_e \sim 10$ eV [53,55] in reasonable agreement with the previously measured nanosecond laser breakdown plasma pressures $\sim 10^5$ bar [22]. For comparison, our measurement of the shock-wave speed in water averaged over the 4.4-mm path (≈ 2.4 km/s $> C_{l,w} \approx 1.5$ km/s) enable estimates of $P_{plas,cr}$, assuming the simple radial attenuation dependence with the exponent $k \approx 1$ (i.e., neglecting dissipative losses) and the initial apparent plasma radius $y_{las}/2 \approx 40$ μm, and using the tabulated pressure dependence of shock-wave speed [38] or its functional form from Ref. [12]. The resulting estimate $P_{plas,cr} \approx 4.5 \times 10^5$ bar (the corresponding initial speed of shock wave ≈ 9 km/s) is qualitatively consistent with the scaling predictions for $P_{plas,cr}$ above, while a simple extrapolation of the narrow prepulse amplitudes $P \approx 2-4$ bar measured by the transducer at the full transit distance from the laser waist pressure, $y_{break}+h \approx 10$ mm, to the same initial apparent plasma radius $y_{las}/2 \approx 40$ μm in assumption of the same radial attenuation dependence, gives unsatisfactory magnitudes $\sim 10^{2-3}$ bar. Therefore, combinations of optical and acoustic techniques may be generally highly advantageous for a comprehensive characterization of opaque laser breakdown plasmas and resulting shock waves.

Next, we discuss the acoustic generation mechanism underlying the appearance of the main compressive pulse in the acquired acoustic transients. Besides the fluence (intensity) dependence of their amplitude P_{comp} in Fig. 6, indicating some relation of these pulses to subcritical and critical water plasmas with energy densities $\varepsilon \sim 1$ kJ/cm^3, sufficient for explosive boiling in water [43,52], we would like also to emphasize the surprising fact that the 100-ns FWHM of the pulses (Fig. 5) is much higher than that of the 25-ns incident laser pulses. From our previous measurements we know that in this study the acoustic transducer and the transit water layer do not introduce any considerable broadening to the acoustic transients [43,56]. Hence, this discrepancy can be ascribed to the acoustic generation on temporal and/or spatial scales larger than those for the initial laser energy deposition during τ_{las} over the focal volume $\approx (x_{las} y_{las} z_{las})$. It is noteworthy that for $F \geqslant F_{break}$ the main compressive pulses have pronounced unipolar shapes with the accompanying rarefaction post-pulse amplitudes not exceeding 20%–30% of P_{comp} (Fig. 5). This ratio of compression-rarefaction pulse amplitudes is characteristic of detection in the acoustic near field from the acoustic source with the diffraction parameter $[y_{break}/L_{D,w}(10\ \text{MHz}) + h/L_{D,FS}(10\ \text{MHz})] \sim 0.1-1$ [44], even despite of their low characteristic frequency ≈ 10 MHz resulting in the much lower diffraction lengths in water and FS, $L_{D,w/FS}(10\ \text{MHz}) \approx x_{las} z_{las} 10\ \text{MHz}/C_{l,w/FS} \approx 0.25$ and 1 mm, respectively. The abnormally reduced diffraction parameter (compare to its estimate ~ 10 in Sec. II) indicates that the actual size of the acoustic source, providing the 100-ns broad, nearly unipolar main compressive acoustic pulses, is much larger (~ 1 mm^2) than the corresponding laser waist cross section $x_{las} z_{las} \approx 0.03$ mm^2. This suggestion is consistent with previous experimental observations reporting formation of mm-sized steam bubbles from micron-sized plasmas during ns laser breakdown in water at comparable pulse energies and focusing conditions [12,13,21,22]. Therefore, the main compressive acoustic pulses can be related to formation of cavitation steam bubbles, rather than to the preceding water microplasma, with their 1-μs-long collapse-rebound cycles at $t_{tr}=4-6$ μs observable in the acquired acoustic transients (Fig. 2).

The pulse amplitudes $P_{comp} \leqslant 15$ bar measured at the transit distance $y_{break}+h \approx 10$ mm from the laser waist correspond to the source pressures $P_{source} \sim 10^2$ bar, assuming the radial attenuation $P(r) \propto 1/r$ and taking the maximum bubble size ~ 1 mm, as derived above from the diffraction considerations. The estimated pressure is surprisingly large, being comparable to the critical pressure of water ≈ 224 bar [38] and indicating, potentially, a significant nonthermal ("chemical") pressure contribution from free radicals produced by the ns laser pulses in water via multiple reactions (2) discussed below. This suggestion is supported by our observations of the sub-mm-deep lateral thermoacoustic generation in surrounding water heated by the longer-wavelength (>200 nm) bremsstrahlung plasma emission, while its shorter-wavelength fraction (<200 nm) provides photodissociation [51] of the strongly absorbing water molecules in the close proximity to the plasma. Moreover, such additional post-ionization "chemical" evolution step, intermediate between the plasma and thermal cavitation dynamics, was directly observed on a subnanosecond time scale during femtosecond laser breakdown in water (see the second expansion stage in Fig. 3 in Ref. [18]), presumably resulting in the generation of the sonic wave.

It is well known that 248-nm laser irradiation provides dissociation of water molecules to free radicals—mostly OH and H ones—via several pathways [32,34,41,42,57,58]. The radicals are directly photogenerated via TPA with $\approx 10\%$ yield [32] [reaction (2a)], but much more significant production rapidly occurs in solvation shells of laser-generated e-i pairs via a detachment reaction of ions [32,34,57] and a dissociative electron attachment [58] [reactions (2b) and (2c), respectively],

$$H_2O \xrightarrow{2\hbar\omega,e} OH + H, \tag{2a}$$

$$H_2O^+ \xrightarrow{H_2O} H_3O^+ + OH, \tag{2b}$$

$$H_2O + e^- \rightarrow OH^- + H, \tag{2c}$$

$$OH \xrightarrow{\hbar\omega} [O + H] \xrightarrow{H_2O} 2OH + H, \tag{2d}$$

with their conjugate reverse reactions and direct association of H, O, and OH radicals [32]. The photochemical dissociation of radicals [32] [reaction (2d)] provides their duplication on the I-dependent time scale $\tau_{dis} = \hbar\omega/(\sigma_{OH} I) \approx 100\ \text{ns}/I$ [GW/cm^2] for the linear absorption cross section $\sigma_{OH} \approx 10^{-20}$ cm^2 estimated from the linear absorption coefficient $\alpha_{OH} \approx 420$ cm^{-1}/mole at 267 nm [42]; for our 25-ns laser pulses the photomultiplication of radicals in water starts for $I > I_{break}$.

Additionally, the reaction (2a) may also occur in water molecules under impact of TPI-seeded hot free (nonsolvated) electrons. Maximum thermal energy k_BT_e of a free electron in a laser field with $I \sim 1$ GW/cm^2 approaches to 10 eV on a picosecond time scale (the corresponding quiver energy ≈ 1 meV and amplitude $\approx 10^{-2}$ Å) via collisions with its parent ion and neutral molecules in water [47]; the hot electron can easily break or ionize neighboring and distant water species via their direct inelastic collisions or photodissociation by the short-wavelength bremsstrahlung radiation of the electron, respectively. The electron impact dissociation channel in water (≈ 6.6 eV/OH bond in H_2O molecules [32,51]) predominates over the more energetic ionization one (≈ 10 eV/electron-ion pair for H_2O molecules in liquid water [32,51]), in contrast to the 248-nm laser-induced TPA and TPI in water molecules [32]. This is also true for dissociation and/or ionization of daughter products, such as OH, OH^+, and H_2O^+, exhibiting gas-phase dissociation energies (5–7 eV) substantially lower, than their ionization potentials (>12 eV) [51]. As a result, laser heating of free electrons in water via the inverse bremsstrahlung effect is terminated in the range of 20–28 eV (the factor of 4 with respect to the corresponding dissociation energies comes from the momentum and energy conservation laws for the gas-phase electron impact process) until complete dissociation of water molecules around primary photogenerated molecular ion-electron pairs via the set of reactions in (2). The dissociation finally results in formation of atomic gas nanobubbles around each central O^+ or H^+ ions (both have the similar first ionization potentials $I_{p1} \approx 13$ eV [38,51]).

When the first and second coordination shells around the primary TPI-generated electron-ion pairs are filled in by gaseous H and O atoms, free electrons in the center of the nanobubbles can be further heated by the laser radiation to higher thermal energies >20–28 eV initiating impact ionization in the gas (atomic ionization by the short-wavelength bremsstrahlung plasma radiation occurs at lower thermal electron energies $k_BT_e \approx 10$–12 eV, but is a very unlikely process). The necessity for such gaseous shell formation via the dissociation of host water molecules around each TPI-generated electron-ion pair prior to the beginning of impact ionization imposes an obvious threshold requirement on laser fluence (intensity) for either femtosecond, or nanosecond laser pulses, and provides a sharp breakdown threshold. Since all condensed matter demonstrates sharp optical breakdown thresholds, the prebreakdown dissociation of host molecules in liquids and soft matter materials seems to be a quite universal induction effect during optical breakdown (in solids the dissociation may be replaced by self-trapping of carriers and subsequent point defect generation [26]). Furthermore, since dissociation of a water molecule into atoms require an overall energy exceeding its first ionization potential and the ratio of fragments to ions should be very high (»1) prior to optical breakdown to support its laser-induced avalanche, the contribution of the dissociation process to the overall optical breakdown energy balance may be more significant, than that of ionization [35].

In subcritical water plasma with density $N_e \sim 10^{22}$ cm^{-3} comparable to the molecular density of water $N_{mol} \approx 3.3 \times 10^{22}$ cm^{-3}, such individual nanobubbles covering coordination spheres of 6–12 atoms around each electron-ion pair, coalesce to form a single micrometer-scale, expanding gas cavity observable visually or via its acoustic emission. In contrast, at lower plasma densities in the prebreakdown regime ($F < F_{break}$), a cloud of numerous separate gaseous nanobubbles may form, being optically and acoustically invisible, but exhibiting considerable highly localized thermal, mechanical, and cytogenic effects on organic molecules and biological structures during tissue dissection or intracellular surgery [2–7,22,23].

C. Comparison to femtosecond laser breakdown in water

The characteristic exponents $K \approx \frac{3}{4}$ observable in bulk pure water for compressive acoustic pulse amplitudes over broad ranges of pulse energies—1–10^2 μJ and 10–10^2 μJ [15], correspond to singly ionized subcritical plasmas [$N_e \sim 10^{21}$ cm$^{-3} \leq N_{crit}(800\ \text{nm}) \approx 2 \times 10^{21}$ cm^{-3}] produced by the tightly focused 800-nm femtosecond and picosecond laser radiation. Energy densities deposited in the plasmas are as low as $\sim 10^{2-3}$ J/cm^3 (one order of magnitude lower, than at the 248-nm laser breakdown in water), being sufficient for rapid (potentially, explosive near-spinodal) nucleation of single steam bubbles at nanosecond and microsecond time scales [52]. Weak shock waves may accompany deposition of the energy densities, being driven by corresponding plasma pressures $P_{plas} < 10$ kbar much lower, than the Mbar plasma pressure magnitudes estimated in Ref. [15], and making optical detection of such shock waves hardly possible [15,18]. The relatively low-energy densities of the plasmas cause their rapid relaxation via expansion and recombination, producing much higher density of free radicals through impact of hot Auger electrons, photodissociation by recombination radiation and the above-mentioned ion-molecule reactions; moreover, even larger quantities of radicals can be produced in prebreakdown regimes prior to avalanche ionization of water molecules via their impact dissociation by hot electrons and photodissociation by short-wavelength bremsstrahlung plasma radiation. The role of free radicals in the energy balance of femtosecond laser-induced breakdown in water, and their chemical cytogenic impact on biological structures may be unexpectedly more significant, than was assumed so far.

V. CONCLUSIONS

In conclusion, we have used optical transmission and contact broadband photoacoustic techniques to identify the optical breakdown, subcritical and critical electron-ion plasma regimes and their main attributes (bubble formation, generation of shock waves, bremsstrahlung plasma emission) during micrometer-scale nanosecond uv laser irradiation of bulk pure water, and to estimate their basic parameters, using the well-known universal scaling relationships between basic plasma and laser parameters. Based on these and previous experimental results, we emphasize the roles of dissociation of water molecules via multiple paths as the induction effect

on initiation of electron avalanches and their energy balance in prebreakdown regimes, and of formation of opaque subcritical plasmas as the final stage of electron avalanche evolution described well by the above-mentioned universal plasma scaling relationships.

[1] D. Song, M. H. Hong, B. Lukyanchuk, and T. C. Chong, J. Appl. Phys. **95**, 2952 (2004).
[2] S. H. Chung, D. A. Clark, C. V. Gabel, E. Mazur, and A. D. Samuel, BMC Neurosci. **7**, 30 (2006).
[3] M. S. Hutson and X. Ma, Phys. Rev. Lett. **99**, 158104 (2007).
[4] V. Venugopalan, A. Guerra, K. Nahen, and A. Vogel, Phys. Rev. Lett. **88**, 078103 (2002); A. Vogel, N. Linz, S. Freidank, and G. Paltauf, *ibid.* **100**, 038102 (2008).
[5] A. Heisterkamp, I. Z. Maxwell, E. Mazur, J. M. Underwood, J. A. Nickerson, S. Kumar, and D. E. Ingber, Opt. Express **13**, 3690 (2005).
[6] R. F. Steinert and C. A. Puliafito, *The Nd:YAG Laser in Ophthalmology. Principles and Clinical Practice of Photodisruption* (Saunders, Philadelphia, 1986).
[7] D. X. Hou, D. L. Butler, M. L. He, and X. Y. Zheng, Lasers Med. Sci.(to be published).
[8] T. Kaji, S. Ito, H. Miyasaka, Y. Hosokawa, H. Masuhara, C. Shukunami, and Y. Hiraki, Appl. Phys. Lett. **91**, 023904 (2007).
[9] P. Testud-Giovanneschi, A. P. Alloncle, and D. Dufresne, J. Appl. Phys. **67**, 3560 (1990).
[10] A. Philipp and W. Lauterborn, J. Fluid Mech. **361**, 75 (1998).
[11] A. Vogel and W. Lauterborn, J. Acoust. Soc. Am. **84**, 719 (1988).
[12] A. Vogel, S. Busch, and U. Parlitz, J. Acoust. Soc. Am. **100**, 148 (1996).
[13] A. Vogel, J. Noack, K. Nahen, D. Theisen, S. Busch, U. Parlitz, D. X. Hammer, G. D. Noojin, B. A. Rockwell, and R. Birngruber, Appl. Phys. B: Lasers Opt. **68**, 271 (1999).
[14] F. Courvoisier, V. Boutou, C. Favre, S. C. Hill, and J.-P. Wolf, Opt. Lett. **28**, 206 (2003).
[15] E. N. Glezer, C. B. Schaffer, N. Nishimura, and E. Mazur, Opt. Lett. **22**, 1817 (1997).
[16] W. Liu, O. Kosareva, I. S. Golubtsov, A. Iwasaki, A. Becker, V. P. Kandidov, and S. L. Chin, Appl. Phys. B: Lasers Opt. **76**, 215 (2003).
[17] V. V. Temnov, K. Sokolowski-Tinten, P. Zhou, A. El-Khamhawy, and D. von der Linde, Phys. Rev. Lett. **97**, 237403 (2006).
[18] C. B. Schaffer, N. Nishimura, E. N. Glezer, A. M.-T. Kim, and E. Mazur, Opt. Express **10**, 196 (2002).
[19] C. Sarpe-Tudoran, A. Assion, M. Wollenhaupt, M. Winter, and T. Baumert, Appl. Phys. Lett. **88**, 261109 (2006).
[20] M. Sakakura, M. Terazima, Y. Shimotsuma, K. Miura, and K. Hirao, Opt. Express **15**, 5674 (2007).
[21] J. Noack, D. X. Hammer, G. D. Noojin, B. A. Rockwell, and A. Vogel, J. Appl. Phys. **83**, 7488 (1998).
[22] A. Vogel and V. Vanugopalan, Chem. Rev. (Washington, D.C.) **103**, 577 (2003).
[23] A. Vogel, J. Noack, G. Hüttman, and G. Paltauf, Appl. Phys. B: Lasers Opt. **81**, 1015 (2005).
[24] S. M. Milas, J. Y. Ye, T. B. Norris, K. W. Hollman, S. Y. Emelianov, and M. O'Donnel, IEEE Trans. Ultrason. Ferroelectr. Freq. Control **50**, 517 (2003).
[25] S. I. Kudryashov, V. D. Zvorykin, A. A. Ionin, V. Mizeikis, S. Joudkazis, and H. Misawa, Appl. Phys. Lett. **92**, 101916 (2008).
[26] V. Mizeikis, S. Joudkazis, H. Misawa, S. I. Kudryashov, V. D. Zvorykin, and A. A. Ionin (unpublished).
[27] M. Li, S. Menon, J. P. Nibarger, and G. N. Gibson, Phys. Rev. Lett. **82**, 2394 (1999).
[28] C. W. Carr, M. D. Feit, A. M. Rubenchik, P. De Mange, S. O. Kucheyev, M. D. Shirk, H. B. Radousky, and S. G. Demos, Opt. Lett. **30**, 661 (2005).
[29] A. S. Epifanov, Sov. Phys. JETP **40**, 897 (1975).
[30] P. K. Kennedy, IEEE J. Quantum Electron. **31**, 2241 (1995).
[31] B. Rethfeld, Phys. Rev. B **73**, 035101 (2006).
[32] C. G. Elles, I. A. Shkrob, R. A. Crowell, and S. E. Bradforth, J. Chem. Phys. **126**, 164503 (2007).
[33] M. Mero, J. Liu, W. Rudolph, D. Ristau, and K. Starke, Phys. Rev. B **71**, 115109 (2005).
[34] D. N. Nikogosyan, A. A. Oraevsky, and V. I. Rupasov, Chem. Phys. **77**, 131 (1983); M. H. Niemz, *Laser-Tissue Interactions: Fundamentals and Applications* (Springer, Berlin, Heidelberg, 2004).
[35] C. A. Sacchi, J. Opt. Soc. Am. B **8**, 337 (1991).
[36] M. D. Feit, A. M. Komashko, and A. M. Rubenchik, Appl. Phys. A: Mater. Sci. Process. **79**, 1657 (2004).
[37] C. R. Phipps, Jr., T. P. Turner, R. F. Harrison, G. W. York, W. Z. Osborne, G. K. Anderson, X. F. Corlis, L. C. Haynes, H. S. Steele, and K. C. Spicochi, J. Appl. Phys. **64**, 1083 (1988).
[38] I. S. Grigor'ev and E. Z. Meilikhov, *Fizicheskie Velichini* (Energoatomizdat, Moscow, 1991).
[39] *Handbook of Optical Constants of Solids*, edited by E. D. Palik (Academic, Orlando, 1991).
[40] A. Dragomir, J. G. McInerney, D. N. Nikogosyan, and A. A. Ruth, IEEE J. Quantum Electron. **38**, 31 (2002).
[41] O. Baghdassarian, H.-C. Chu, B. Tabbert, and G. A. Williams, Phys. Rev. Lett. **86**, 4934 (2001).
[42] S. O. Nielsen, B. D. Michael, and E. J. Hart, J. Phys. Chem. **80**, 2482 (1976).
[43] S. I. Kudryashov, K. Lyon, and S. D. Allen, Phys. Rev. E **75**, 036313 (2007).
[44] V. E. Gusev and A. A. Karabutov, *Laser Optoacoustics* (AIP, New York, 1993).
[45] V. D. Zvorykin, Laser Part. Beams (to be published).
[46] X. A. Shen, S. C. Jones, and P. Braunlich, Phys. Rev. Lett. **62**, 2711 (1989).
[47] N. I. Koroteev and I. L. Shumay, *Physics of High-Power Laser Radiation* (Moscow, Nauka, 1991).
[48] C. V. Shank, R. Yen, and C. Hirlimann, Phys. Rev. Lett. **50**, 454 (1983).
[49] A. Dubietis, E. Kucinkas, G. Tamosauskas, E. Gaizauskas, M. A. Porras, and P. Di Trapani, Opt. Lett. **29**, 2893 (2004).

[50] S. I. Kudryashov, K. Lyon, and S. D. Allen, J. Appl. Phys. **100**, 124908 (2006).
[51] *Thermodynamic Properties of Individual Substances*, edited by V. P. Glushko (Moscow, Nauka, 1979).
[52] R. K. Shori, A. A. Walston, O. M. Stafsudd, D. Fried, and J. T. Walsh, Jr., IEEE J. Sel. Top. Quantum Electron. **7**, 959 (2001).
[53] N. G. Basov, O. N. Krokhin, and G. V. Sklizkov, Reports of FIAN USSR Vol. 52, p. 71, (1970) (in Russian).
[54] R. A. Graham, *Solids Under High-Pressure Shock Compression* (Springer, Berlin, 1993).
[55] J. F. Ready, *Effects of High Power Laser Radiation* (Academic, Orlando, 1971).
[56] S. Paul, S. I. Kudryashov, K. Lyon, and S. D. Allen, J. Appl. Phys. **101**, 043106 (2007).
[57] C. L. Thomsen, D. Madsen, S. R. Keiding, J. Thogersen, and O. Christiansen, J. Chem. Phys. **110**, 3453 (1999).
[58] A. Mozumder, Phys. Chem. Chem. Phys. **4**, 1451 (2002).